TECHNICAL ARTICLE

Effect of Multi-directional Forging on the Evolution of Microstructural and Mechanical Properties of Lightweight Al-Cu-Li Alloy AA2050

C. Jagadeesh [ORCID], H. Shivananda Nayaka, S. Ramesh, and T.R. Praveen

Microstructural evolution and the mechanical properties of recently developed lightweight AA2050 Al-Cu-Li alloy have been presented. A processing route of multi-directional forging (MDF) at 170 °C followed by artificial aging at 150 °C was employed. Systematic EBSD analysis revealed significant grain refinement with grain size reducing from 74.3 ± 12 to 22.1 ± 2.8 μm after 12 passes of MDF. Transformation of deformation bands into subgrains with dynamic recrystallization has led to grain refinement. TEM results show the presence of large dislocation clusters and deformation bands in MDF processed samples with a large number of fine precipitates in peak aged MDF processed samples. XRD analysis shows variation in peak intensities and occurrence of peak shifts due to induced lattice strain upon MDF. A substantial increase in microhardness and strength was observed with a minor trade-off with ductility after 12th MDF pass. Further, enhancement in strengths and microhardness were observed in post-MDF aged samples. Experimental results show the combined effect of strain hardening, grain size reduction, and precipitate hardening which influence the material strength. A combination of MDF and artificial aging has shown great potential to enhance the strength and ductility of AA2050.

1. Introduction

Lightweight aluminum alloys possess high specific strength and have always attracted the aircraft and aerospace industries in complex structural applications as they directly influence efficiency and thus reduce operational costs. Al-Li alloys were shown to be more potential in recent literature. For every 1 wt.% Li addition to an aluminum alloy, a 3% reduction in density with an almost 7% increase in elastic modulus can be obtained (Ref 1). This reduction in density with a simultaneous increase in strength has led to various developments in Al-Li alloys and evolved into three generations involving the optimization of alloy compositions. With this breakthrough, AA2050 Al-Cu-Li alloy has gained large research interest due

to its superior strengths, high fracture toughness, better corrosion resistance, and less anisotropic properties compared to its predecessors (Ref 2). It also exhibits greater potential with no apparent limitations for cryogenic applications in the aerospace sector (Ref 3).

Microstructural modifications through severe plastic deformation (SPD) have proven to be a promising technique leading to significant improvements in strength, corrosion resistance, and tribological properties in various Al alloys (Ref 4-8). By employing a suitable SPD technique, one can obtain high strength and high ductility by tailoring microstructure (Ref 9). Various SPD processes such as Equal Channel Angular Pressing (ECAP) (Ref 10), High-Pressure Torsion (HPT) (Ref 11), Accumulative Roll Bonding (ARB), Constrained Grove Pressing (CGP), and Multi-Directional Forging (MDF) induce large plastic strains in a crystal lattice, which results in the formation of new crystallographic defects, results in microstructural modifications. Grain size reduction, formation of dislocation clusters, deformation bands, and fragmentation of secondary particles are commonly observed phenomenon in SPD processed materials. However, the observed phenomenon is highly dependent on the intrinsic material characteristics such as alloying systems, initial grain size, stacking fault energies, critical resolved shear stress, and SPD processes adopted (Ref 9, 12). Among the various developed SPD processes, MDF is known to be simple, and effective, adding the ability to operate at the required temperature (Ref 13). By MDF large strains can be induced in a wide range of metals and alloys, and the required setup has a simple die design with a hydraulic press or any high compression unit. Also, one can continuously monitor the increase in strain rate during the process between the passes.

Aging is a process of inducing precipitates in an alloy by diffusion of solute atoms into matrix and formation of clusters

C. Jagadeesh and H. Shivananda Nayaka, Severe Plastic Deformation Laboratory, Mechanical Engineering, National Institute of Technology Karnataka, Surathkal 575025, India; S. Ramesh, Department of Mechanical Engineering, RV Institute of Technology and Management, Karnataka, Bengaluru 560075, India; and T.R. Praveen, Severe Plastic Deformation Laboratory, Mechanical Engineering, National Institute of Technology Karnataka, Surathkal 575025, India; and Central Research Facility, National Institute of Technology Karnataka, Surathkal 575025, India. Contact e-mails: jagadeeshc807@gmail.com, hsn@nitk.edu.in, ramaghalli@gmail.com, and praveentr0@gmail.com.

known as precipitates with their own lattice structure, tailoring the material and mechanical properties. Pre-straining before exposure to aging has shown a large influence on mechanical properties and aging kinetics in age-hardenable Al alloys (Ref 14, 15). S. Cheng et al. reported as cryorolling of AA2024 Al alloy before artificial aging supports uniform nucleation and growth of nano-sized precipitates, leading to a significant increase in strength and ductility (Ref 6). Similarly, Zhao et al. (Ref 8) reported a simultaneous increase in strength and ductility due to large dislocation accumulation during cryo rolling and fine distribution of secondary particles post-aging in AA7075 Al alloy. Accelerated precipitation kinetics and enhanced strengths were reported by Hockauf et al. after peak aging of pre-ECAP processed AA6056 Al alloy (Ref 16). Similarly, Gubicza et al. reported an improved strength of ECAP processed Al-Zn-Mg alloy due to fine dispersion of η-phase precipitates after aging (Ref 50). T. Aoba et al. observed the increase in strengths and ductility during post-MDF aging of 6XXX series Al alloy with better age-hardenability when aged at relatively low temperatures (Ref 17). Reduction in grain size and induced dislocation clusters during SPD process greatly accelerate the nucleation of precipitates and their growth at the early stage of aging, thus reducing the formation of copper depletion regions at the grain boundaries, thus preventing the formation of precipitation-free zones (PFZ) (Ref 18). It was understood that SPD processing prior to aging of precipitate hardenable alloys resulted in a fine and in-homogeneous distribution of precipitates with the absence of PFZ zones. Fine precipitates prevented recrystallization by obstructing grain boundary motions through Zener pinning effect, thus increasing the ability of the alloy to perform at high temperatures (Ref 51).

In the present work, AA2050 Al-Cu-Li alloy is processed by MDF at elevated temperature to induce large strains and MDF processed alloy was further exposed to aging at constant temperature by varying the exposure time. Mechanical characterization has been carried out to understand the effect of MDF on aging by microhardness and tensile tests. Microstructure characterization such as electron backscattered diffraction (EBSD) and x-ray diffraction (XRD) has been carried out to understand the mechanism between process and strengths. Studies on Al alloys processed by various SPD processes followed by artificial aging treatments do exist in the literature and are limited to conventional Al alloys only (Ref 19-21, 26). However, studies on the effect of MDF, post-MDF aging on Al-Cu-Li alloys, and microstructural evolution upon the same are rarely reported.

2. Experimentation

AA2050 Al-Cu-Li alloy was procured from Bharat Aerospace Alloys Pvt Ltd, India with a nominal composition as Al-3.5Cu-0.85Li-0.36 Mg-0.35Mn-0.05Zn-0.1Zr (wt.%) determined using inductively coupled plasma optical emission spectrometry (ICP-OES). The alloy was in the form of 50-mm-thick slabs of which several 24 × 30x30 mm rectangular parallelepiped samples are extracted. As illustrated in the processing route line diagram (Fig. 1a), as-received alloy was first subjected to solution heat treatment (SHT) at a temperature of 510 ± 5 °C for 90 min, followed by water quenching to room temperature and this sample condition is referred to

"SHT" hereafter. SHT samples are subsequently subjected to MDF up to 12 passes at 170 ± 5 °C in a specially designed die setup. A split type die with a central cavity of 30 mm × 30 mm × 80 mm made of hardened steel incorporated with heating cartridges and a thermocouple attached to a control panel to maintain constant temperature is used in the process. As illustrated in Fig. 1(b), MDF process involves compression of the alloy by sequential changing of loading direction along the three mutually perpendicular axes of the sample. During the 1st MDF pass, sample was compressed along the X-axis (Face A). The sample, after 1st pass, has rotated such that the Y-axis becomes the new compression axis and is compressed along face B and termed as 2nd pass. Similarly, during 3rd pass, sample is compressed along Z-axis by aligning the sample's Z-axis to the compression axis (face C). The compression along all three axes completes one cycle and imparts a strain of approximately 0.8 (~ 0.26 per pass). Further sets of SHT and MDF processed samples are subjected to artificial aging carried out in a salt bath furnace and isothermally held at 150 ± 2 °C for various time intervals up to 80 h.

Specimens from MDF processed samples for various characterizations were extracted at the midsections, perpendicular to the sample's last forged axis. MDF processed samples are characterized for microstructural analysis using EBSD. Sample preparation for EBSD analysis involves manual polishing by standard metallographic procedure to obtain a scratch-free mirror-like polished surface, followed by electropolishing at 15 V for 15 s maintained at -20 °C using an electrolyte of 75% ethanol + 25% phosphoric acid. Orientation image mapping (OIM) was extracted from Field Emission Scanning Electron Microscope (Zeiss Gemini 300) with EDAX Electron Back-Scatter Diffraction (EBSD) attachment. Postprocessing of EBSD data was carried out using TSL OIM™ software (version 7.0). Structural characterization using x-ray diffraction (XRD) technique was carried out on a Malvern Panalytical's Empyrean Diffractometer operating at 40 kV and 40 mA equipped with Cu-Kα source for 2θ range of 10° to 100° in steps of 0.02°. Tensile specimens were extracted at the midsections parallel to the last forging axis and prepared as per ASTM: E8 sub-size standard with 16 mm gauge length and 6 mm gauge diameter. A uniaxial tensile test was carried out with a constant strain rate of 2×10^{-4} s^{-1} on a Tinius Olsen machine of 25 kN capacity (S-Series, H25K-S). Vicker's Micro hardness was carried out on mirror-like surface polished samples with five indentations per sample condition at different locations to retain the accuracy of results.

3. Results and Discussion

3.1 Microstructural Characterization

3.1.1 Electron Backscattered Diffraction (EBSD) Analysis. Orientation Image Micrographs (OIMs) of 6th and 12th pass MDF processed, MDF + aged samples including SHT condition are extracted from the EBSD studies and are presented in Fig. 2. OIM are superimposed with image quality map with high angle grain boundaries (HAGB) where misorientation angle θ ≥ 15° and low-angle grain boundaries (LAGB) with misorientation angle θ < 15°. Inset in Fig. 2 represents inverse pole figure (IPF) map of crystallographic
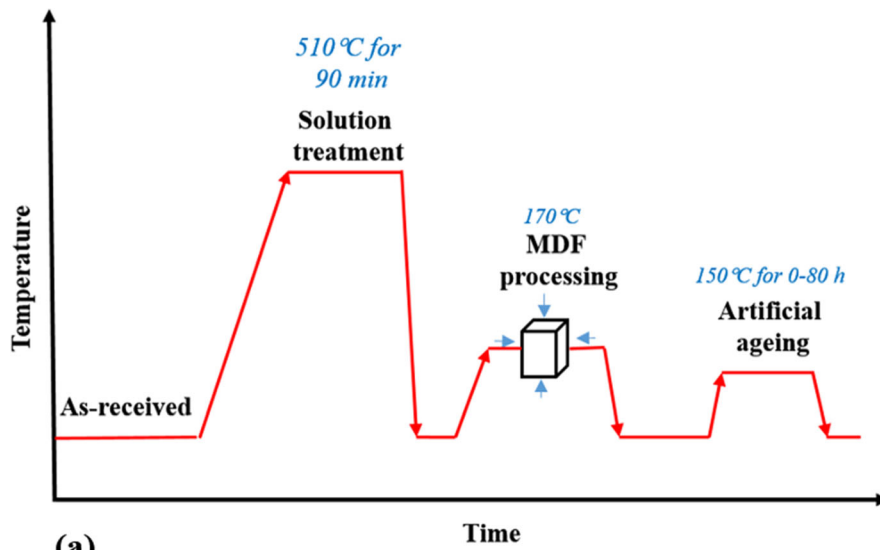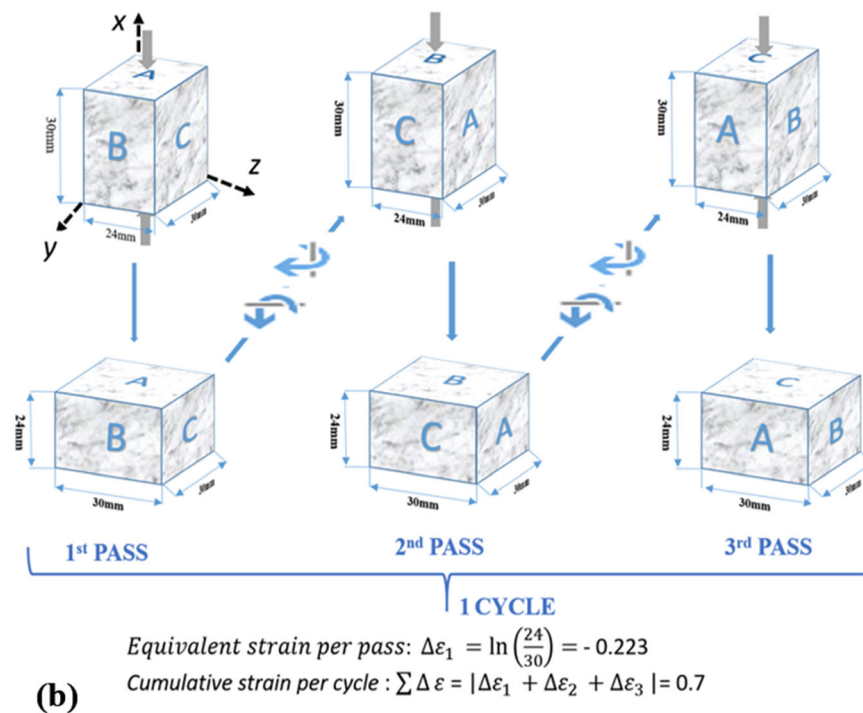
Fig. 1 (a) Processing route undergone in the current study, (b) schematic illustration of multi-directional forging process

directions of grains that are parallel to the last forging axis. OIM of SHT revealed the presence of elongated coarse grains (CGs) with a larger fraction of HAGBs (Fig. 2a) and grain size distribution plot Fig. 3(a), further confirming the existence of a high fraction of CGs and fewer fine grains.

Figure 2(b) refers to the 6th pass MDF processed sample, where initial grains are fragmented by shear bands and/or deformation bands. An increase in cumulative strain at every pass has influenced the increase in misorientation angles of subgrain boundaries from to HAGBs as observed in Fig. 2(c) at region-1 in 12th pass sample. Width of the subgrains formed by fragmentation of coarse grains is observed to be approximately 10 μm, and careful examination of the microstructures of 12th pass sample indicated as region 2 in Fig. 2(c) reveals the presence of new grains with a diameter of few microns. The

occurrence of continuous dynamic recrystallization at higher cumulative strains promoted new Ultra Fine Grains (UFG) due to restoration and recovery (Ref 27, 28). Various researchers reported the formation of UFGs at cross-overs of micro-shear bands at higher strains (Ref 29, 30). Thus, the overall microstructure developed in 12th pass sample is a combination of subgrains formed by the transformation of deformation bands and UFGs formed due to dynamic recrystallization. Peak aged 6th and 12th pass processed samples shown in Fig. 2(d, e) represent similar microstructure as observed in un-aged counterparts indicating no further occurrence of recrystallization or microstructural changes during aging. Further, an overall observation of OIMs of all processed conditions does not show any preferred orientation of crystallographic planes.
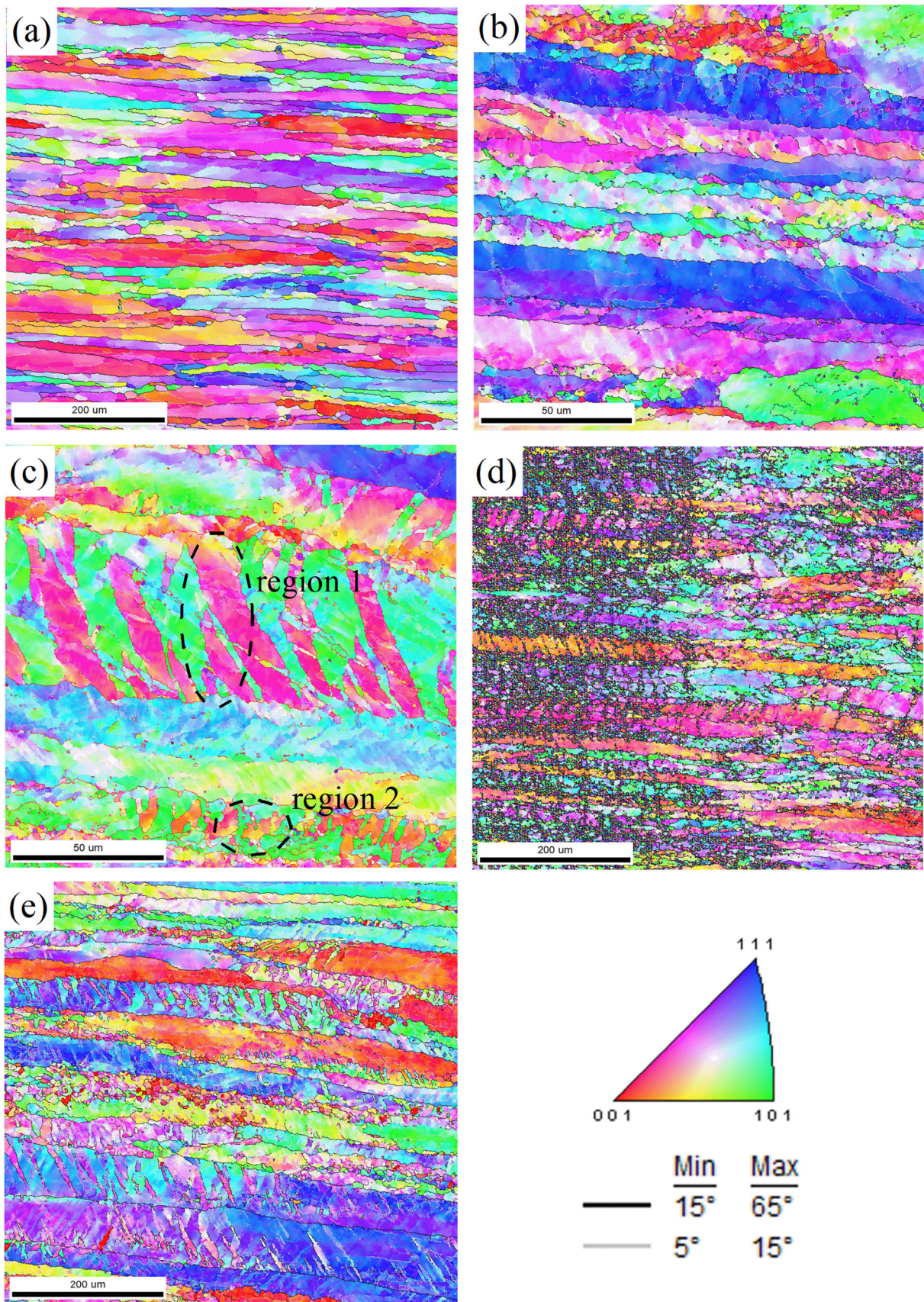
Fig. 2 EBSD generated orientation image micrographs of AA2050 alloy after (a) SHT, (b) 6 pass, (c) 12 pass, (d) 6 pass + peak aged, and (e) 12 pass + peak aged conditions
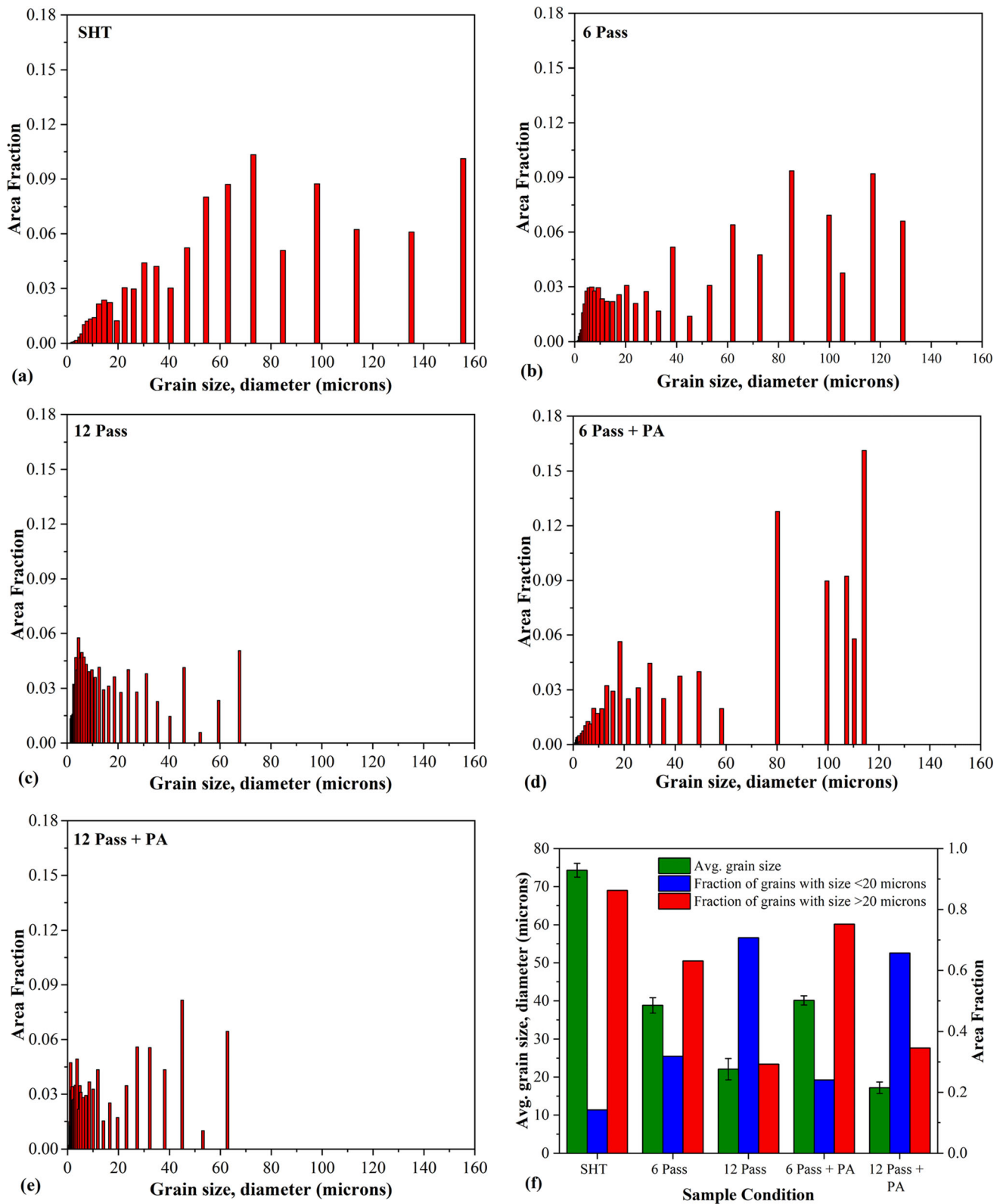
Fig. 3 (a-e) Grain size distribution plots for various processed conditions, (f) comparison of grain size distribution in various processed conditions

3.1.2 Grain Size Distribution. Figure 3(a-e) represents the grain size distribution plots of various processing conditions that appear to be bi-modal distribution. Grains having a size lesser or equal to 20 μm are considered as fine grains and greater than 20 μm as coarse grains, and a comparison of the same for various processed conditions is shown in Fig. 3(f).

SHT sample shows a large fraction of coarse grains (approx. 86%) and fewer fine grains with an average grain size of 74.3 ± 12 microns. It was observed that MDF has resulted in the reduction in average grain size, with 38.81 ± 8 and 22.1 ± 2.8 μm from 6th pass to 12th pass samples, respectively. The fraction of fine grains was increased from $\sim 14\%$ (SHT) to $\sim 31\%$ in 6th pass and $\sim 70\%$ in 12th pass samples and is represented in Fig. 3(f). However, microstructures of artificially peak aged samples reveal no significant effect on grain refinement or grain growth, where average grain size of 40.12 ± 2 and 17 ± 2 μm is observed for peak aged conditions on 6th and 12th pass MDF processed samples.

3.1.3 Misorientation Angle and Grain Boundary Character Distribution (GBCD). GBCD plots obtained by considering the individual number fraction of LAGBs and HAGBs and misorientation angle distribution plots for samples processed at different conditions are shown in Fig. 4. SHT sample has a high fraction of HAGBs due to the presence of recrystallized grains (Ref 16), with misorientation distributed over a wide range (Fig. 4a). After 6th pass of MDF, a considerable amount of increase in LAGBs with a decrease in HAGBs was observed, and average misorientation shifting to lower angles (from Fig. 4b,c), due to formation of deformation bands and subsequent transformation into subgrains. It is worth noting that from 6 to 12th pass of MDF processing shows a slight increase in the fraction of HAGBs, which is in contrast with SHT to 6th pass sample. With an increase in cumulative strain from 6 to 12th pass, the misorientation of the subgrains formed during initial passes increases and transforms into HAGBs with simultaneous formation of UFGs due to the occurrence of continuous dynamic recrystallization as discussed in previous sections (Ref 31, 33). Figure 4(a, e, f) represents the post-MDF peak aged samples showing similar misorientation characteristics to their un-aged counterparts as aging was carried out well below MDF processing temperature.

3.1.4 Kernel Average Misorientation (KAM) and Grain Orientation Spread (GOS). Intra-grain misorientation parameters such as kernel average misorientation (KAM) and grain orientation spread (GOS) generated from EBSD data, to estimate the strain accumulation within and across the grains for various processing conditions, are shown in Fig. 5. KAM is an average misorientation at the center of the kernel, calculated by considering the average of local misorientation between the center and points on the perimeter of the kernel and excluding the misorientation greater than $5°$ (Ref 32). Similarly, GOS is calculated by taking an average of misorientations, determined by measuring the misorientation angle between each measuring point and the overall average misorientation angle of grain (Ref 34, 35).

A higher number of fractions were observed at low angles of KAM for SHT Sample, which indicates less strain within the grain due to the large fraction of recrystallized grains (Ref 36) and this was also noticed in Fig. 4(a). Similarly, in Fig. 5(b), GOS values of SHT samples are observed at low angles representing the low dislocation content and strain-free grains. From Fig. 6(a, b) for 6th pass MDF processed sample, KAM and GOS peaks were broader and observed slightly ahead of SHT peak ensuring higher dislocation content. 12th pass sample followed similar characteristics as of 6th pass sample with a small decrease in average KAM and GOS at higher strains, due to dynamic recrystallization (Ref 36, 37).

3.1.5 TEM Analysis. Figure 6 shows the bright-field TEM micrographs of AA2050 Al-Cu-Li in different processed conditions. Large dislocation densities and deformation bands are evident in the 6th pass MDF processed sample as seen in Fig. 6a. Similarly, as evident in Fig. 6b, 12th pass MDF processed sample revealed dislocation tangles at the grain and subgrain boundaries. The observed large density of dislocations and dislocation clusters are due to the large induced strains during MDF process.

Figure 6(c) displays a bright-field TEM micrograph of SHT + Peak aged sample consisting of large number of needle-shaped intragranular T1 precipitates in grain interiors. In addition, grain boundaries are decorated with continuous intergranular GB precipitates. Proton et al. reported similar microstructure during artificial aging of AA2050 Al alloy (Ref 52). Formation of continuous large precipitates at the grain boundaries and T1 precipitates at the grain interiors results in copper depletion regions adjacent to grain boundaries causing PFZs.

Bright-field TEM micrograph of 12th pass MDF + peak aged sample is shown in Fig. 6(d). It reveals the presence of fine needle-shaped intragranular T1 precipitates in grain interiors with smaller discontinuous GB precipitates in contrast to conventionally aged samples (SHT + Peak aged). Large dislocations densities observed in the MDF processed sample act as the preferential sites for the nucleation T1 precipitates, thus a large number of fine precipitates were seen in MDF + peak sample. Similar results of plastic deformation prior to aging promoting nucleation of T1 precipitates were reported by Cassada et al. and Gable et al. in Al-Cu-Li alloys (Ref 53, 54).

3.2 X-Ray Diffraction

XRD patterns extracted for SHT, MDF processed, and post-MDF peak aged samples are shown in Fig. 7. All phases identified through XRD belong to face-centered cubic (FCC) system and peaks corresponding to Al of all processing conditions are indexed to (111), (220), (322), (432) and (640) hkl lattice planes. From Fig. 7(a), variations in peak intensities are observed upon MDF processing resulting from the formation of subgrains, change in the crystal orientations, and fine grains. Further, for more insight, peak analysis of Al (111) plane occurring at 2θ of $38.5°$ for SHT and MDF processed samples are presented in Fig. 7(b). Shifting of peaks toward the left (lower 2θ angle) was observed, due to the accumulation of strains with MDF passes (Ref 38, 39). Further width of the peaks was observed to be broadening with an increase in the number of MDF passes as an effect of reduction in crystallite size, work hardening, and residual stresses (Ref 39, 40). Figure 7(a) also represents the XRD patterns at peak aged conditions of SHT, 6th, and 12th pass MDF processed samples subjected to artificial aging heat treatment at 150 °C. Analysis of peaks showed small intensities of peaks corresponding to Al_3Li, Al_2CuLi, and Al_2Cu precipitates, confirming the formation of secondary particles upon artificial aging. Less change in peak intensities is observed in comparison with their corresponding un-aged counterparts indicating no significant changes occurring in crystal orientations during artificial aging.
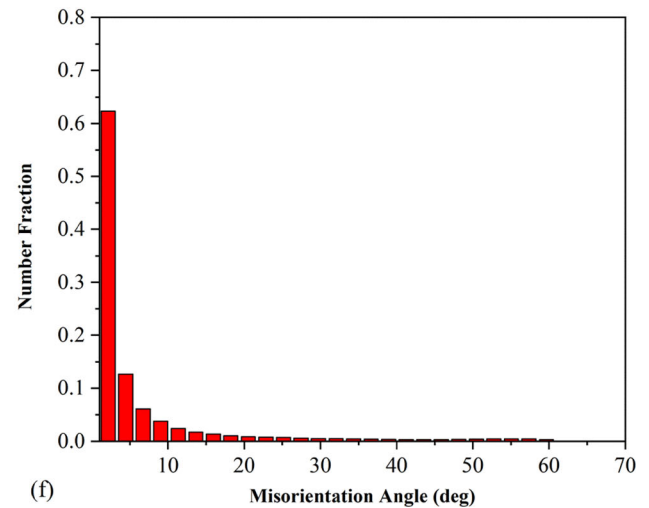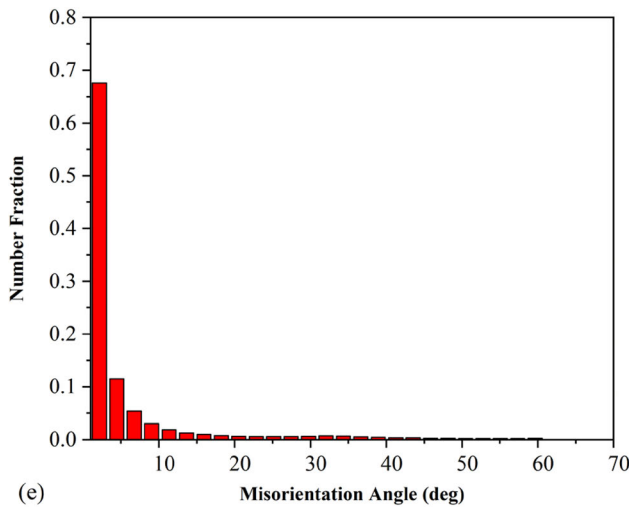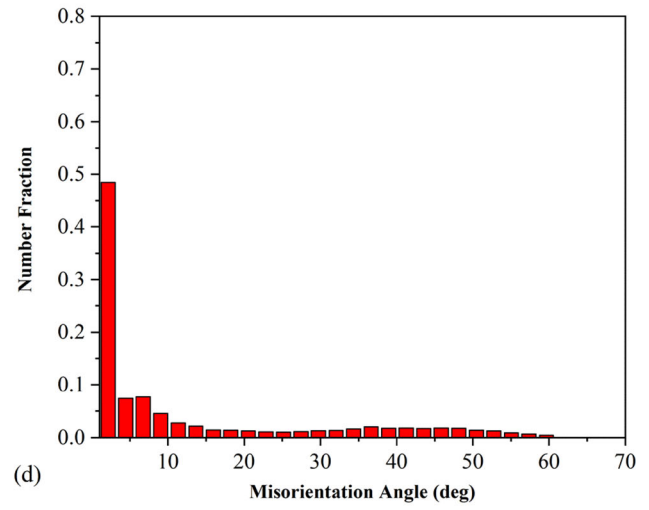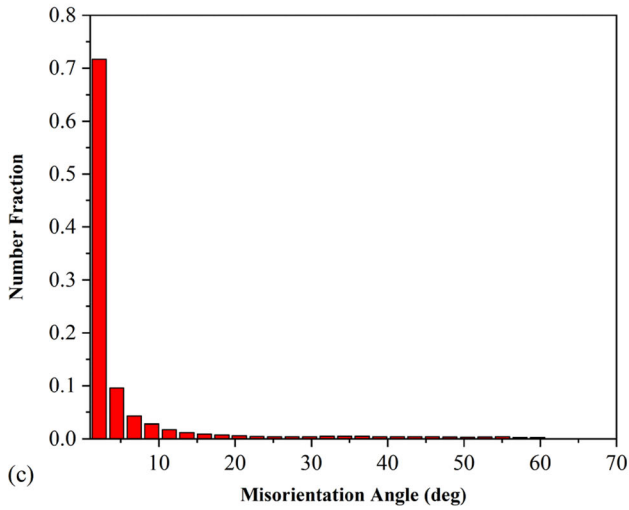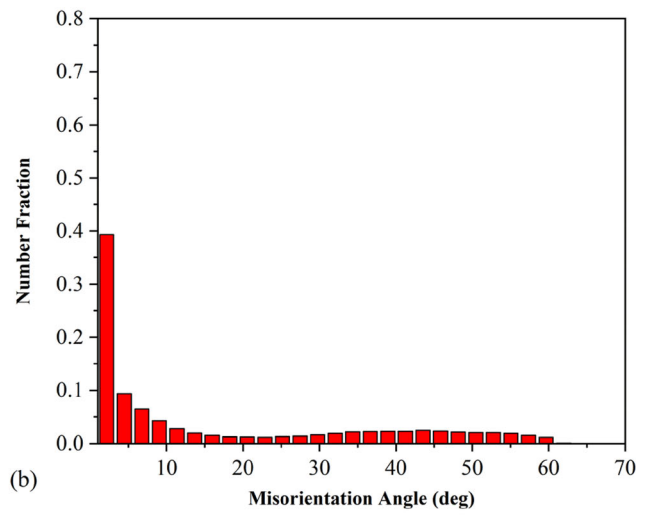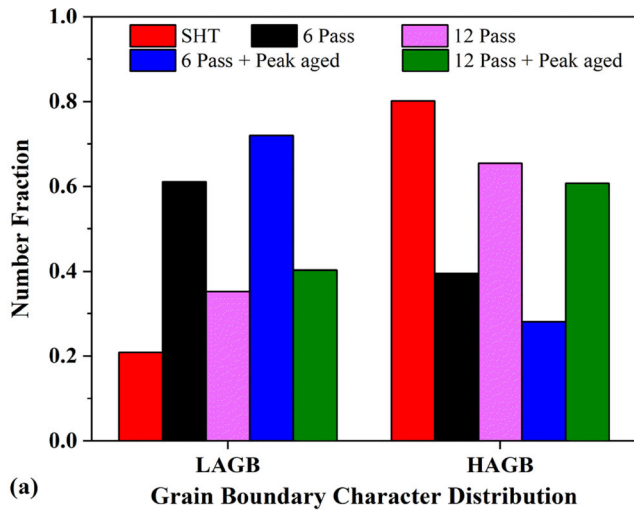
Fig. 4 **a** Grain boundary character distribution, Misorientation angle distribution for **b** SHT, **c** 6 pass, **d** 12 pass, **e** 6 pass + peak aged, **f** 12 pass + peak aged sample conditions

3.3 Microhardness

Figure 8(a) shows the results of Vicker's microhardness test of SHT and MDF processed samples. SHT samples showed a hardness of 80 HV and increased to 120, 142, 149 and 153 HV after 3rd, 6th, 9th and 12th pass, respectively. Initially, a significant increase in hardness of 51% from SHT to 3rd pass and 19% from 3rd to 6th pass due to large strain accumulations/work hardening was observed. Further, 5 and 3% increase in hardness for 9th and 12th pass was observed indicating
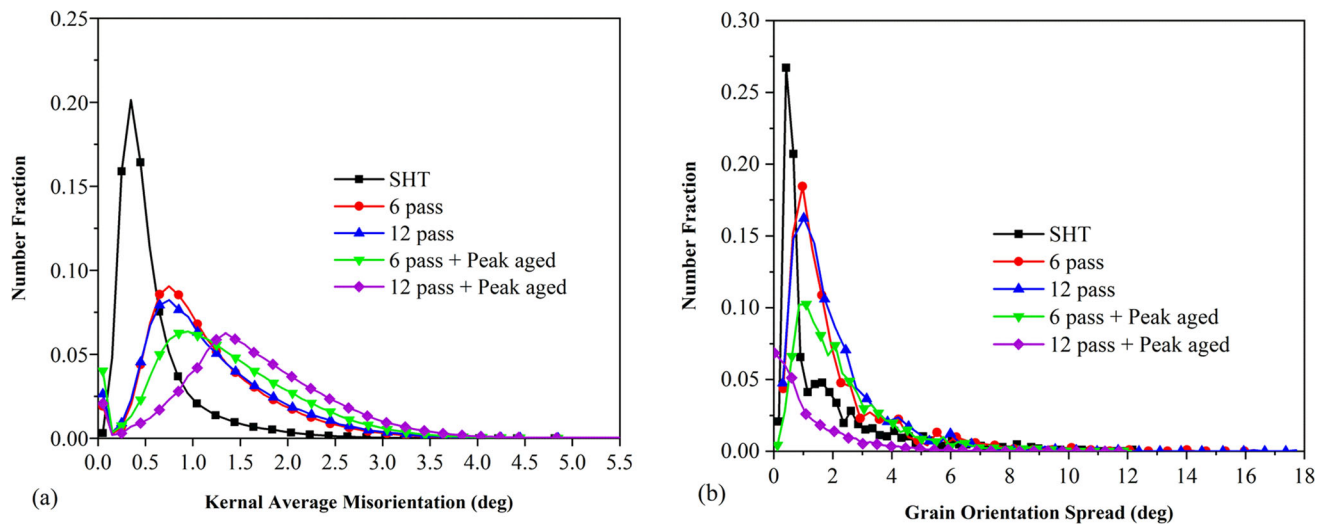
Fig. 5 EBSD generated (a) kernel average misorientation (KAM) plots, (b) grain orientation spread (GOS) plots for various processed conditions

saturation in work hardening. This is due to the occurrence of dynamic recrystallization observed at cumulative higher strains. From Fig. 8(a), it has been noticed that the final hardness was increased by 91% after 12 passes of MDF and this has shown a significant effect on material behavior.

Figure 8(b) shows the comparison of age hardening curves of selected sample conditions (SHT, 6th and 12th pass MDF processed) during artificial aging at 150 °C up to 80 h. SHT samples showed an increasing trend in average hardness values up to 40 h of aging and reported a peak hardness of 152 HV, with no further significant variation up to 72 h. However, in contrast to SHT condition, MDF + aged samples show initial softening characteristics (up to one hour of aging) due to the dissolution of dislocation clusters that occurred during the MDF process (Ref 22, 42). 6th and 12th pass samples reported a peak hardness of 164 HV and 173 HV after 25 and 20 h of aging, respectively. By comparing the results in Fig. 8(b), SHT samples showed longer duration than MDF processed samples in attaining peak hardness, which indicates the enhanced aging kinetics (Ref 4, 5, 43). Further holding of samples post-peak aging for longer durations reveals the over-aging effect, where a reduction in hardness value has been noticed (Ref 44).

3.4 Tensile Properties

Stress–strain curves and their corresponding mechanical properties of the alloy studied in different processed conditions are shown in Fig. 9. Aluminum alloys having FCC crystal structure exhibit good ductility but do not show significant yielding in the plastic region. From Fig. 9(b), it is evident that the yield strength (YS) and ultimate tensile strength (UTS) have significantly increased after MDF processing from 204 and 340 MPa in SHT condition to 500 MPa and 517 MPa in 12th pass MDF processed conditions, respectively. Reduction in elongation from 24% in SHT condition to 10% in 12th pass MDF processed condition was observed. During SPD processing of Al alloys, such an increase in strengths with a trade-off with ductility is more commonly reported in the literature (Ref 34, 41, 45). This behavior of increase in strengths and reduction in ductility with an increase in induced strains during SPD is

attributed to grain boundary strengthening and dislocation strengthening (Ref 34, 46, 47).

Figure 9(c) displays the stress–strain curves of differently processed samples in selected aging conditions. For conventionally peak aged condition (SHT + aging at 150 °C for 40 h), specimens showed YS of 390 MPa and UTS of 447 MPa with 32% elongation. This increase in strength is a common trend, generally observed during aging of solution heat-treated Al alloys due to the precipitation of various strengthening precipitates (Ref 18, 48). 6th and 12th pass post-MDF peak aged samples exhibited an increase in strengths and slightly enhanced ductility when compared to un-aged counterparts. The observed increase in ductility was attributed to the recovery of certain dislocations due to the nucleation and growth of precipitates during artificial aging (Ref 49).

3.5 Effect of Microstructure on Mechanical Properties

As observed in this work, the significant improvement in mechanical properties (strength and microhardness) with increase in MDF passes is closely related to microstructural evolution. It has been inferred from Sect. 3.1.1 that MDF processing led to significant grain refinement. According to the Hall–Petch equation with a decrease in average grain size, yield stress of the material increases (Ref 22, 23). Thus, grain refinement observed upon MDF had a significant effect on strengthening. Other important strengthening mechanisms in SPD processed materials are strain hardening and dislocation strengthening. According to the Taylor relation, with increase in dislocation content, yield strength also increases (Ref 24, 25). In the present study, the peak shifts in XRD profiles as seen in Fig. 7(b) and broader KAM and GOS peaks observed in Fig. 5 indicate the increase in lattice strain and dislocation content with increase in the number of MDF passes. TEM micrographs further validate the presence of large dislocation clusters in 6th and 12th pass MDF processed samples. Thus, the observed significant improvement in strength and hardness is attributed to the combined effect of grain refinement, dislocation strengthening, and strain hardening (Ref 26).
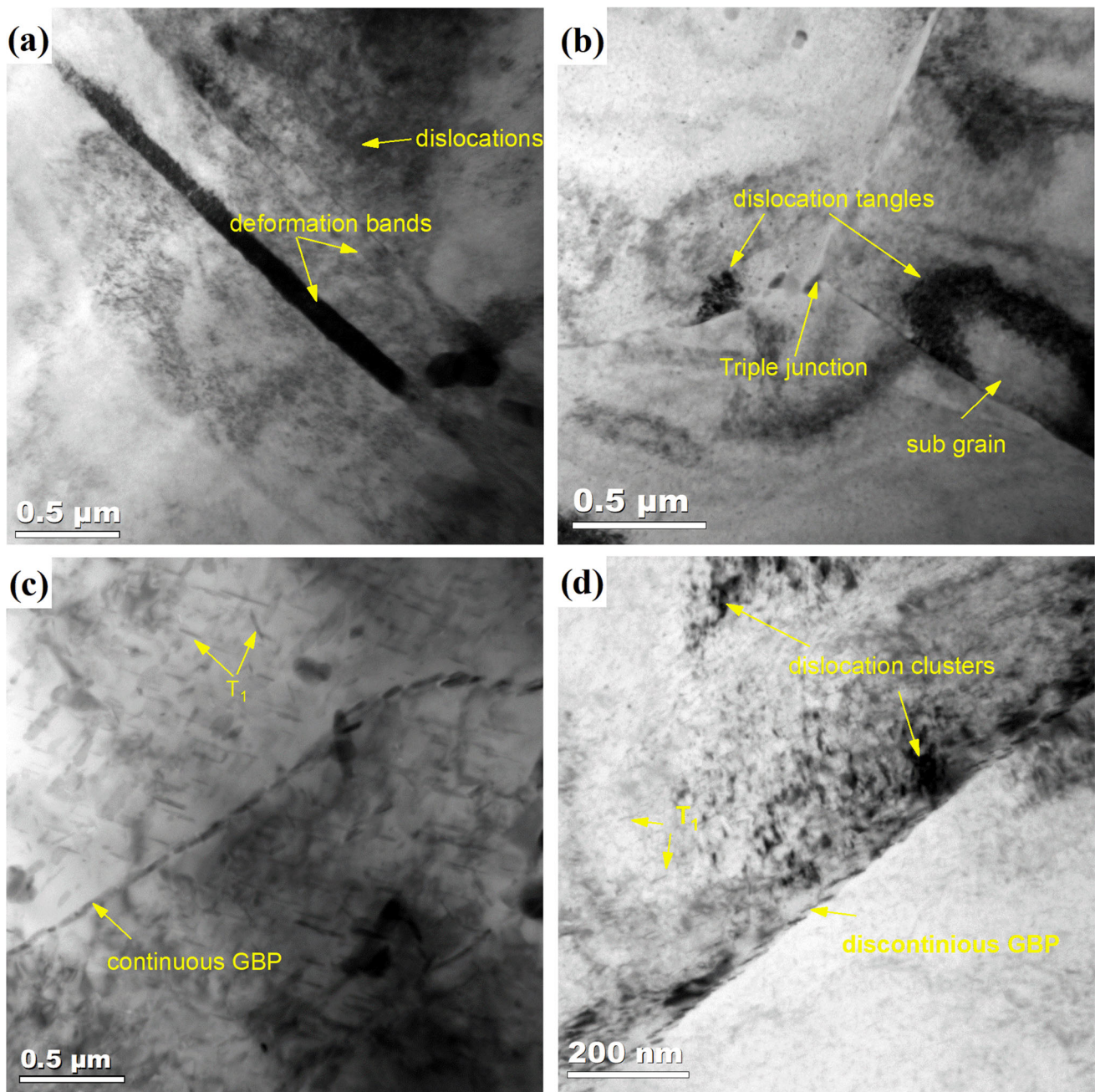
Fig. 6 TEM microstructures of (a) 6 pass MDF processed, (b) 12 pass MDF processed and (c) SHT + peak aged, (d) 12 pass + peak aged AA2050 Al-Cu-Li alloy

From Fig. 3(f), no significant change in average grain size was observed in samples subjected to peak aging post-MDF processing. This is due to the low aging temperature that did not affect grain growth. This confirms that grain size had no further influence on the observed mechanical properties during aging. It is evident in TEM micrographs (Fig. 6) that the dislocation densities decreased after peak aging when compared to non-aged samples. As discussed in the introduction, dislocations act as the nucleation sites for the precipitates and further growth of precipitates happens with the consumption of dislocations. A decrease in dislocation density upon aging could further accumulate more dislocations and probably be the cause for the slight increase in ductility in peak aged post-MDF

processed samples. However, the effect of reduction in dislocation densities on strength properties is significantly less as the precipitate strengthening had highly influenced the mechanical properties (Ref 6). Precipitate strengthening will have a significant effect on mechanical properties as they act as a barrier to dislocation mobility. The factors such as particle/precipitate spacing, average size, and volume fraction influence precipitation strengthening. TEM micrographs as seen in Fig. 6(c, d) show the formation of precipitates in the grain interiors upon aging and are further confirmed in XRD results. However, peak aged sample after 12th pass of MDF processing showed a large density of fine precipitates in the grain interiors compared to the peak aged condition of SHT
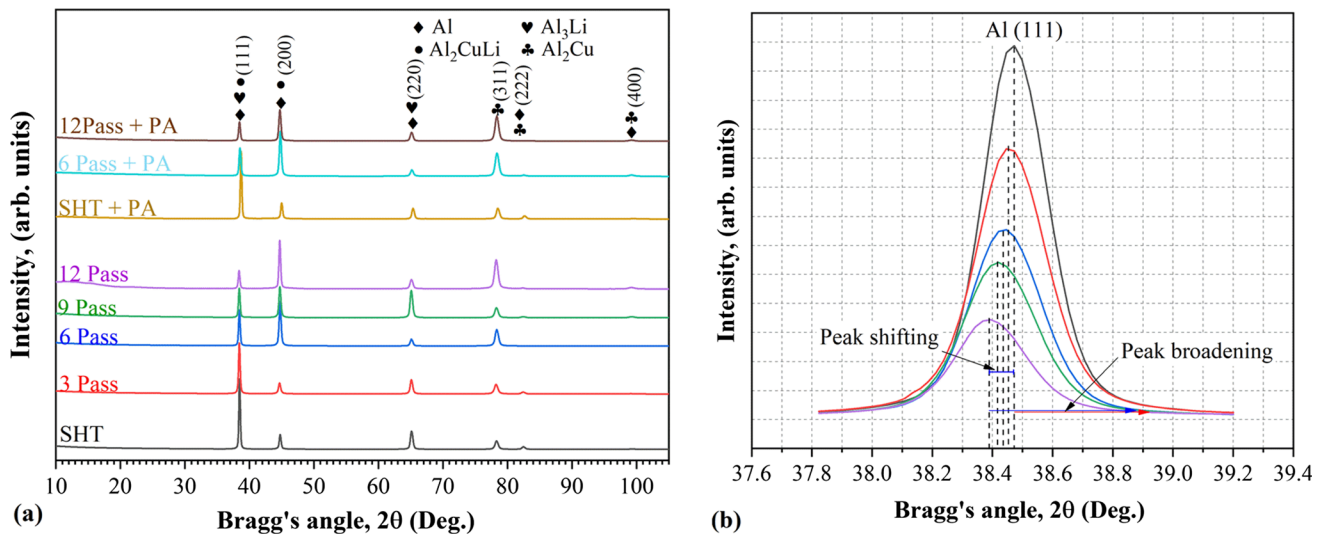
Fig. 7 (a) X-ray diffraction patterns, (b) x-ray diffraction peak profile analysis for peaks corresponding to (111) lattice plane of AA2050 Al-Cu-Li alloy for various processed condition
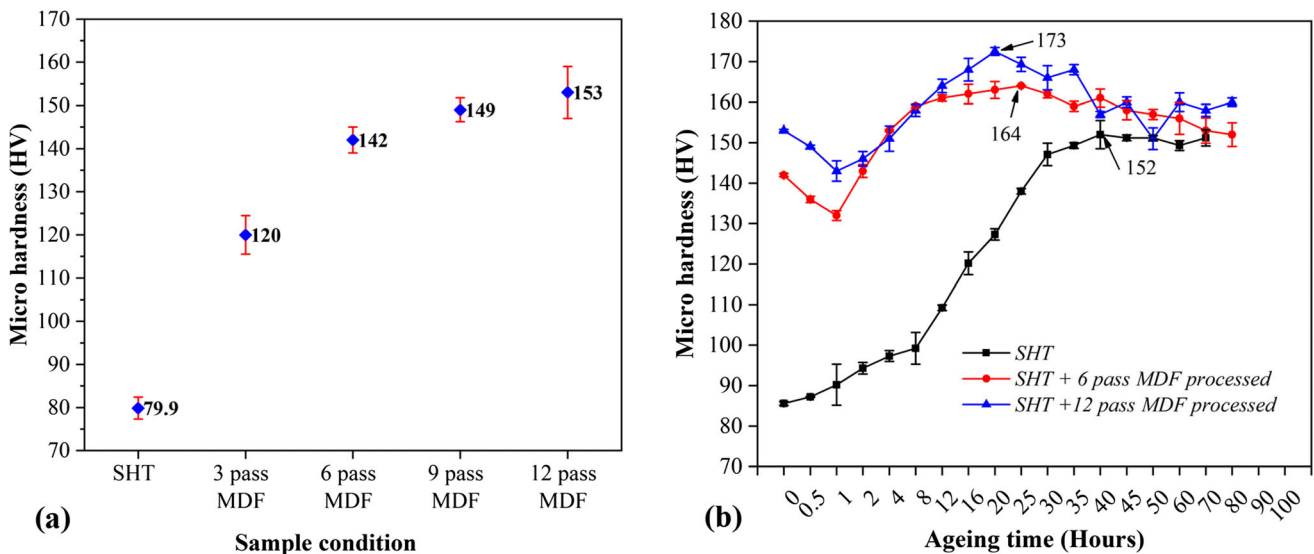

Fig. 8 Change in Vickers's micro hardness of AA2050 Al-Cu-Li alloy (a) with increase in number of MDF passes, (b) as a function of time for artificial aging of SHT, 6 pass and 12 pass MDF processed samples

samples. This shows that precipitate strengthening is more profound in MDF processed samples compared to the non MDF processed sample. Further, from Fig. 5(a), it is evident that KAM plots for 6th and 12th pass peak aged samples showed a broader spread of misorientation compared to unaged counterparts indicating a further increase in lattice strain. This could be due to the strain induced during the growth of precipitates in the crystal lattice. Thus, it can be concluded that, in addition to grain strengthening and strain hardening as an effect of MDF processing, precipitate hardening has led to significant improvements in strength and hardness properties in peak aged samples subjected to MDF.

3.6 Fractography

Fractured surfaces of tensile test samples were examined for fractography to understand the mechanism of fracture. Fig-ure 10 shows the fractured surface of SHT and MDF processed samples. Figure 10(a) shows fractured surface morphologies of SHT sample, where a combination of ductile and brittle fractures was observed. A large number of different sized dimples were identified resulting from the more ductile type fracture and are in good agreement with the ductility observed during a tensile test. Figure 10(a) also shows small dimples along the tear ridges corresponding to brittle fracture or material tear. Figure 10(b) shows the fractured surface of 3rd pass MDF processed sample with a large number of elongated dimples, and the presence of rupture regions indicates transient fracture. It should be noted that the depth of the dimples is reduced when compared to SHT sample. As the 3rd pass MDF sample shows good agreement with an increase in hardness, tensile strength, and decrease in ductility, fractography indicates the transformation of the sample fracture from ductile to
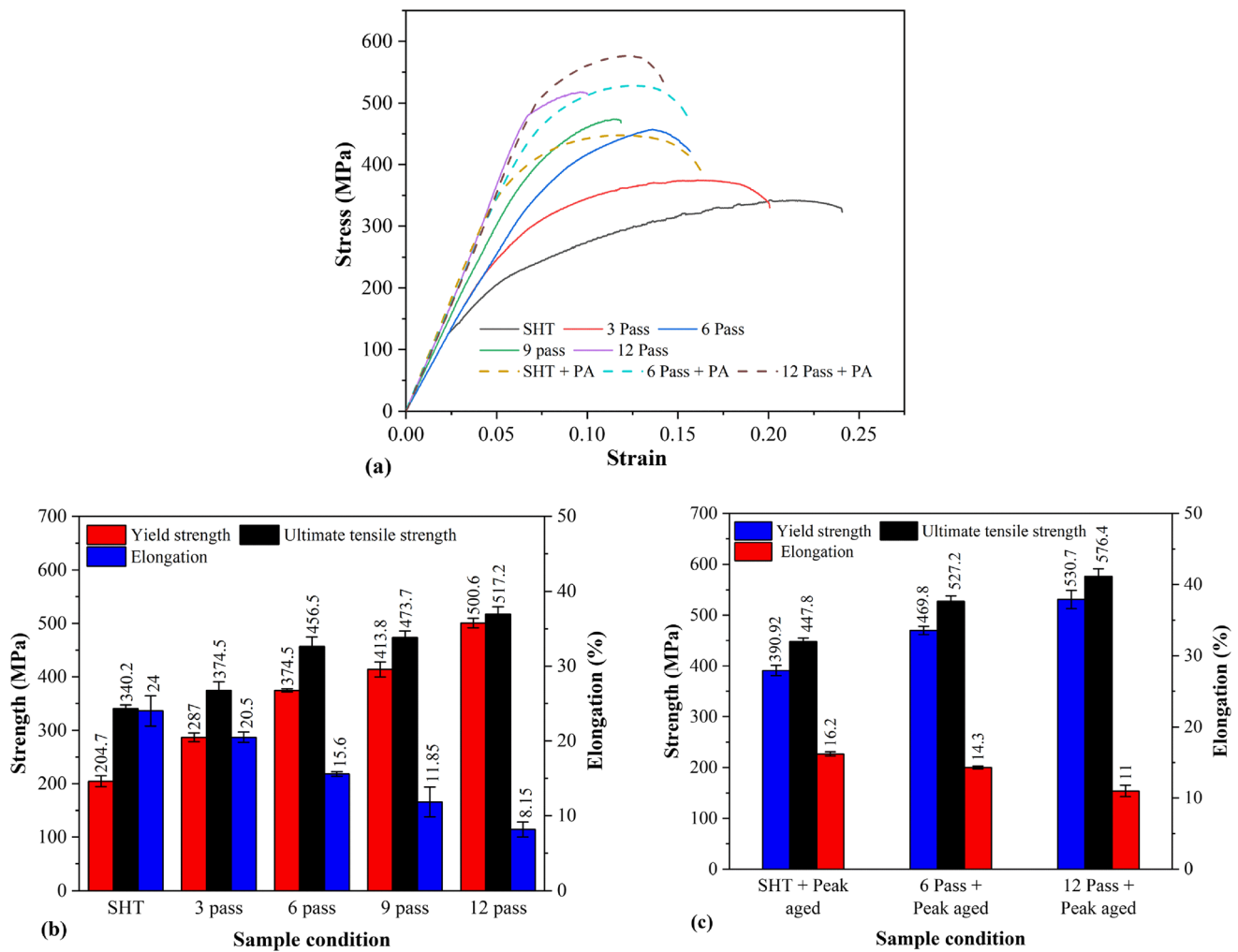
Fig. 9 Tensile stress–strain curves of (a) SHT, MDF processed samples and artificially aged samples for selected conditions. Comparison of mechanical properties of (b) SHT and MDF processed samples and (c) artificially aged samples for selected conditions

brittle due to strain accumulation. Similar features are observed in 6th, 9th and 12th pass processed samples showing relatively large ruptured regions with more tear ridges, respectively, following reduced ductility observed.

Figure 11 shows the fractured surface morphologies of peak aged samples after SHT, 6th and 12th pass MDF processing. Figure 11(a) shows a large number of dimples along with step ridges representing the effect of aging on SHT sample. Figure 11(b) shows the fractured surface of peak aged 6th pass MDF processed sample revealing the combination of clustered dimples and ruptured region. The presence of clustered dimples along the tear ridges is in good agreement with the reduced ductility observed when compared to SHT + peak aged condition. Similarly, Fig. 11(c) shows the fractured surface of 12th pass peak aged sample with long straight ridges by coalescence of small dimples in the pattern of straight lines indicating a mixed mode of fracture with further reduced ductility. The presence of more dimples and less ruptured regions on 6th and 12th pass peak aged samples as seen in Fig. 11(b, c) indicates significant ductility in the samples as compared to un-aged counterparts as seen in

Fig. 10(c, e) and is in good agreement with the increased in ductility observed upon aging.

4. Conclusion

In this article, investigation of AA2050 Al-Cu-Li alloy processed by MDF till 12 passes. Evolution of microstructure and mechanical properties are reported, and the following conclusions were drawn based on experimental results.

1. Fragmentation of coarse laminar grains occurred due to the formation of shear/deformation bands at lower strains and further transformation of these deformation bands into high angle subgrains with gradual increase in misorientation angles at higher strains. Further, at higher strains, fine grains are promoted at the intersections of shear bands due to continuous dynamic recrystallization.
2. TEM microstructure reveals the presence of deformation bands and large dislocation densities in 6 Pass MDF processed samples with dislocations tangled around the sub-
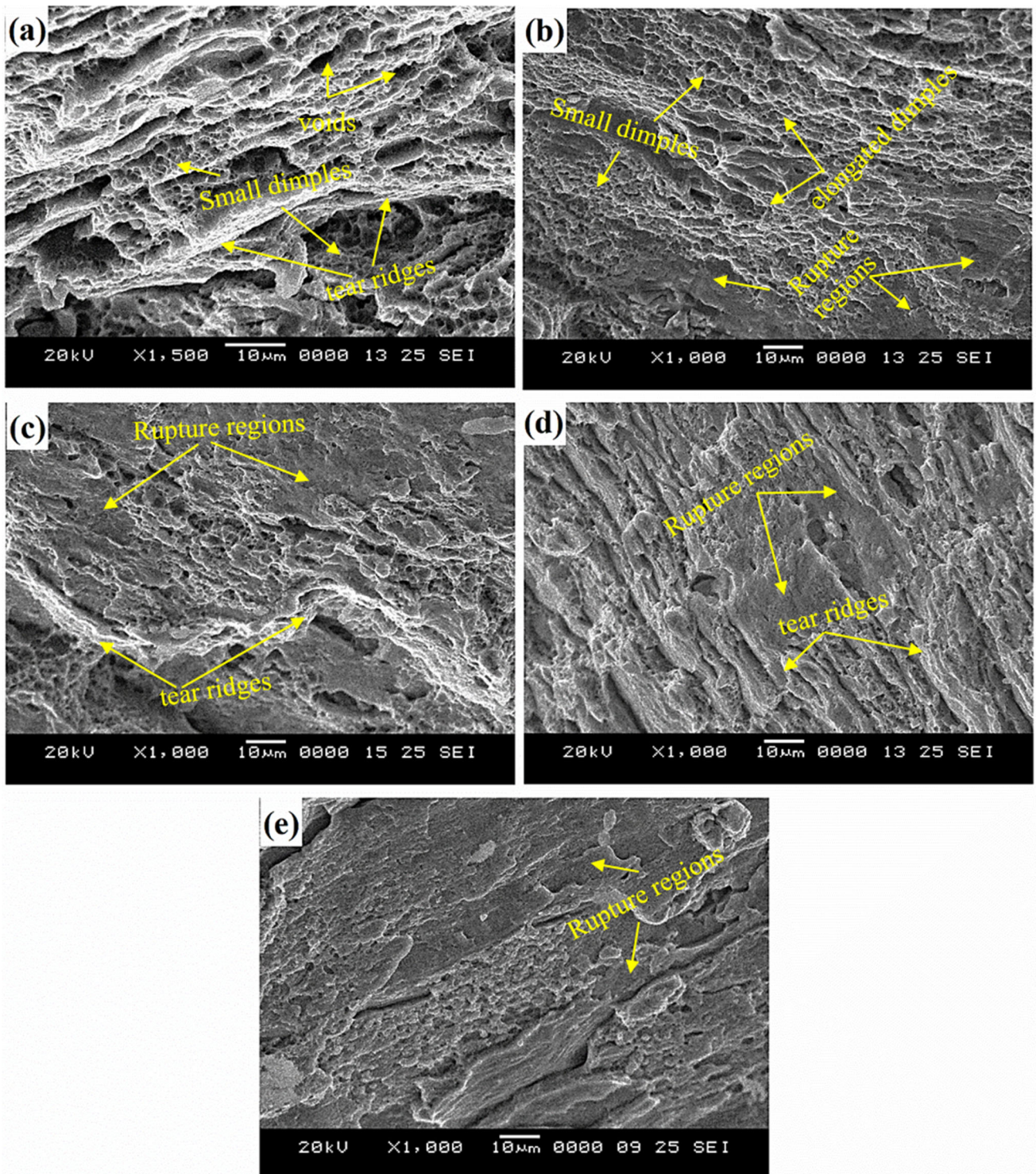
Fig. 10 Tensile fractured surface morphologies of (a) SHT, (b) 3rd pass, (c) 6th pass (d) 9th pass, and (e) 12th pass MDF processed samples

grain and grain boundaries. Further, 12 Pass MDF + peak aged samples showed distribution of finer precipitates and dislocation clusters compared to SHT + PA counterparts.

3. Microhardness shows a significant increase in hardness up to 6 passes from 80 to 142 HV, as a result of work hardening, and a slight increase up to 153 HV after 12 passes. The 12th pass MDF processed sample showed a maximum hardness of 173 HV during post-deformation artificial aging.

4. With increase in number of MDF passes, enhancement in strengths with a trade-off in ductility was observed due to the effect of strain hardening and grain refinement. Meanwhile, artificial aging of MDF samples shows further increase in strengths with slight increase in ductility due to the combined effect of grain refinement, strain hardening and precipitation hardening.
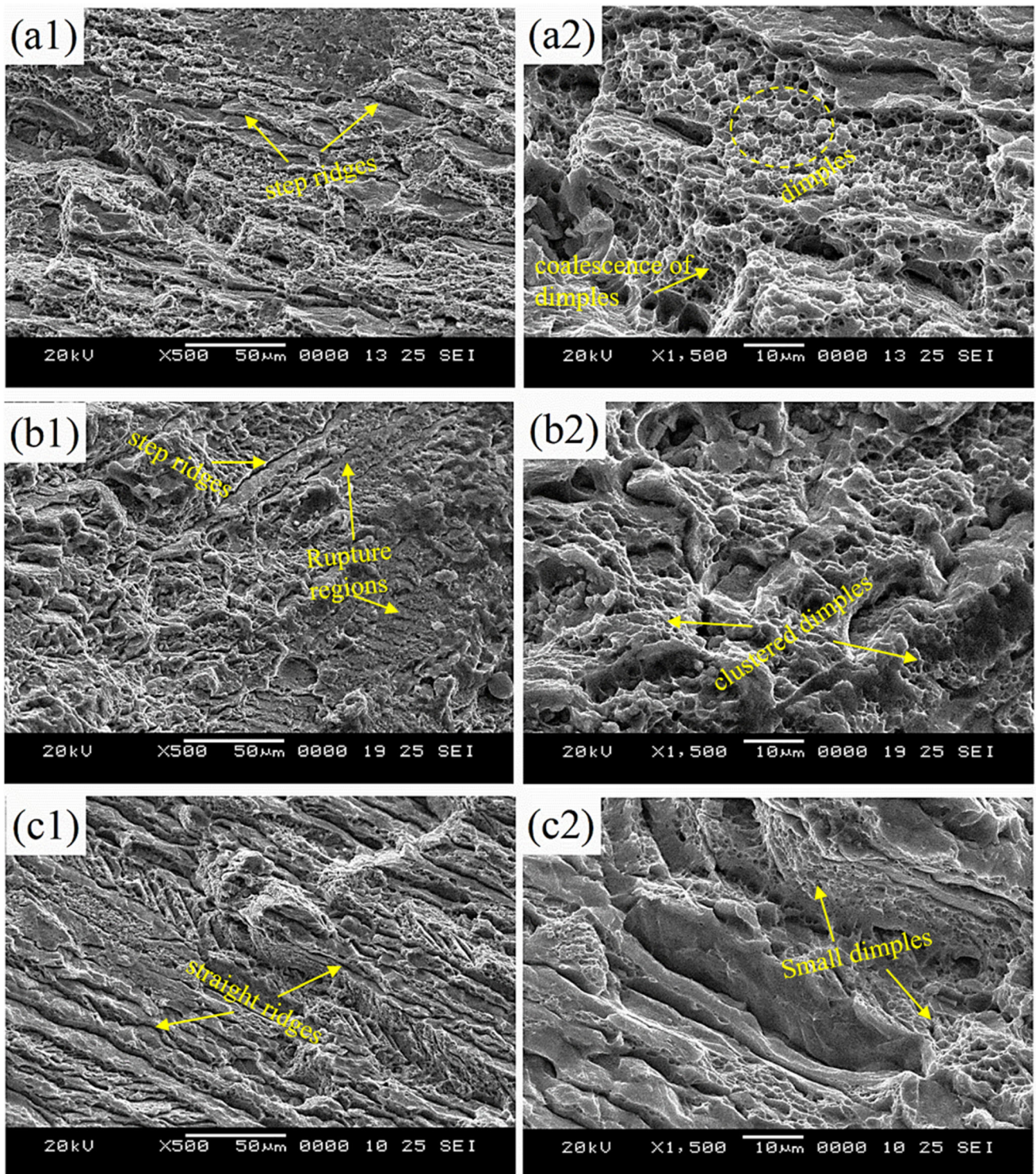
Fig. 11 Tensile fractured surface morphologies of (a) SHT + peak aged, (c) 6 pass MDF + peak aged, and (e) 12 pass MDF + peak aged sample conditions

5. Fractography demonstrates the mixed mode of fracture in differently processed samples, with SHT samples showing the dominance of dimples. Upon MDF processing, with increase in the number of MDF passes, the fractured surface morphologies were dominated by ruptured regions and tearing ridges.

6. Work hardening, high dislocation densities and grain refinement are primary causes of strength improvement in MDF processed samples. Apparently, precipitation hardening enhances material strength on MDF + aged samples.

References

1. P. Rambabu, N. Eswara Prasad, V. V Kutumbarao, and R.J.H. Wanhill, Aluminium Alloys for Aerospace Applications BT - Aerospace Materials and Material Technologies: Volume 1: Aerospace Materials, edited by N.E. Prasad, R.J.H. Wanhill, (Springer, Singapore, 2017), pp. 29–52. https://doi.org/10.1007/978-981-10-2134-3

2. R.J.H. Wanhill, Aerospace Applications of Aluminum-Lithium Alloys, *Aluminum-Lithium Alloy. Process. Prop. Appl.*, 2013 https://doi.org/10.1016/B978-0-12-401698-9.00015-X

3. D.C.V. Kooi, W. Park, and M.R. Hilton, Characterization of Cryogenic Mechanical Properties of Aluminum-Lithium Alloy C-458, *Scr. Mater.*, 1999, **41**(11), p 1185–1190. https://doi.org/10.1016/S1359-6462(99)00264-X

4. T. Shanmugasundaram, B.S. Murty, and V. Subramanya Sarma, Development of Ultrafine Grained High Strength Al-Cu Alloy by Cryorolling, *Scr. Mater.*, 2006, **54**(12), p 2013–2017. https://doi.org/10.1016/j.scriptamat.2006.03.012

5. S. Ramesh, G. Kumar, C. Jagadeesh, G. Anne, and H.S. Nayaka, Effect of Equal Channel Angular Pressing on Properties Evaluation of Biodegradable Mg-Zn-Mn Alloy, *J. Bio- Tribo-Corrosion 2021 72*, 2021, **7**(2), p 1–13. https://doi.org/10.1007/S40735-021-00506-7

6. S. Cheng, Y.H. Zhao, Y.T. Zhu, and E. Ma, Optimizing the Strength and Ductility of Fine Structured 2024 Al Alloy by Nano-Precipitation, *Acta Mater.*, 2007, **55**(17), p 5822–5832. https://doi.org/10.1016/j.actamat.2007.06.043

7. R.Z. Valiev, N.A. Enikeev, M.Y. Murashkin, V.U. Kazykhanov, and X. Sauvage, On the Origin of the Extremely High Strength of Ultrafine-Grained Al Alloys Produced by Severe Plastic Deformation, *Scr. Mater*, 2010, **63**(9), p 949–952. https://doi.org/10.1016/j.scriptamat.2010.07.014

8. Y.H. Zhao, X.Z. Liao, S. Cheng, E. Ma, and Y.T. Zhu, Simultaneously Increasing the Ductility and Strength of Nanostructured Alloys, *Adv. Mater.*, 2006, **18**(17), p 2280–2283. https://doi.org/10.1002/adma.200600310

9. S. Ramesh, G. Anne, G. Kumar, C. Jagadeesh, and H.S. Nayaka, Influence of Ball Burnishing Process on Equal Channel Angular Pressed Mg-Zn-Si Alloy on the Evolution of Microstructure and Corrosion Properties, *SILICON*, 2020 https://doi.org/10.1007/s12633-020-00541-y

10. A.P. Zhilyaev, and T.G. Langdon, Using High-Pressure Torsion for Metal Processing: Fundamentals and Applications, *Prog. Mater. Sci*, 2008 https://doi.org/10.1016/j.pmatsci.2008.03.002

11. V.M. Segal, Severe Plastic Deformation: Simple Shear versus Pure Shear, *Mater. Sci. Eng. A*, 2002, **338**(1–2), p 331–344

12. R.Z. Valiev, R.K. Islamgaliev, and I.V. Alexandrov, Bulk Nanostructured Materials from Severe Plastic Deformation, *Prog. Mater. Sci*, 2000 https://doi.org/10.1016/S0921-5093(02)00066-7

13. M. Hussain, P.N. Rao, D. Singh, R. Jayaganthan, and S. Singh, Comparative Study of Microstructure and Mechanical Properties of Al 6063 Alloy Processed by Multi Axial Forging at 77k and Cryorolling, *Procedia Engineering*, 2014 https://doi.org/10.1016/j.proeng.2013.11.028

14. X. Chen, H. Zhang, and G. Zhao, Precipitation Behavior and Strengthening Mechanism of Extruded 2196 Al-Cu-Li Alloy Plate during Multi-Step Age-Hardening Treatment, *J. Mater. Eng. Perform.*, 2021 https://doi.org/10.1007/S11665-021-06310-1

15. T. Dorin, A. Deschamps, F. De Geuser, W. Lefebvre, and C. Sigli, Quantitative Description of the T1 Formation Kinetics in an Al–Cu–Li Alloy Using Differential Scanning Calorimetry, Small-Angle x-Ray Scattering and Transmission Electron Microscopy, *Philos. Mag.*, 2014, **94**(10), p 1012–1030. https://doi.org/10.1080/14786435.2013.878047

16. K. Hockauf, L.W. Meyer, M. Hockauf, and T. Halle, Improvement of Strength and Ductility for a 6056 Aluminum Alloy Achieved by a Combination of Equal-Channel Angular Pressing and Aging Treatment, *J. Mater. Sci.*, 2010, **45**(17), p 4754–4760. https://doi.org/10.1007/s10853-010-4544-y

17. T. Aoba, M. Kobayashi, and H. Miura, Microstructural Evolution and Enhanced Mechanical Properties by Multi-Directional Forging and Aging of 6000 Series Aluminum Alloy, *Mater. Trans.*, 2018, **59**(3), p 373–379. https://doi.org/10.2320/matertrans.L-M2017856

18. J. Fragomeni, R. Wheeler, and K.V. Jata, Effect of Single and Duplex Aging on Precipitation Response, Microstructure, and Fatigue Crack Behavior in Al-Li-Cu Alloy AF/C-458, *J. Mater. Eng. Perform.*, 2005, **14**, p 18–27. https://doi.org/10.1361/10599490522329

19. W. Yan, X. Liu, J. Huang, and L. Chen, Strength and Ductility in Ultrafine-Grained Wrought Aluminum Alloys, *Mater. Des.*, 2013, **49**, p 520–524. https://doi.org/10.1016/j.matdes.2013.01.019

20. T. Aoba, M. Kobayashi, and H. Miura, Effects of Aging on Mechanical Properties and Microstructure of Multi- Directionally Forged 7075 Aluminum Alloy, *Mater. Sci. Eng. A*, 2017, **700**(June), p 220–225. https://doi.org/10.1016/j.msea.2017.06.017

21. S. Khani, M. Kazeminezhad, and R. Loge, Effect of Concurrent Precipitation on the Texture Evolution during Continuous Heating of Multi Directionally Forged Solution Treated Al-Cu-Mg Alloy, *Mater. Charact.*, 2017, **131**(June), p 399–405. https://doi.org/10.1016/j.matchar.2017.07.033

22. N. Hansen, Hall-Petch Relation and Boundary Strengthening, *Scr. Mater.*, 2004, **51**(8), p 801–806. https://doi.org/10.1016/j.scriptamat.2004.06.002

23. R.A. Masumura, P.M. Hazzledine, and C.S. Pande, Yield Stress of Fine Grained Materials, *Acta Mater.*, 1998, **46**(13), p 4527–4534. https://doi.org/10.1016/S1359-6454(98)00150-5

24. J. Gubicza, N.Q. Chinh, G. Krallics, I. Schiller, and T. Ungar, Microstructure of Ultrafine-Grained Fcc Metals Produced by Severe Plastic Deformation, *Curr. Appl. Phys.*, 2006, **6**(2), p 194–199. https://doi.org/10.1016/j.cap.2005.07.039

25. S. Dadbakhsh, A. Karimi Taheri, and C.W. Smith, Strengthening Study on 6082 Al Alloy after Combination of Aging Treatment and ECAP Process, *Mater. Sci. Eng A*, 2010, **527**(18), p 4758–4766. https://doi.org/10.1016/j.msea.2010.04.017

26. T. Aoba, M. Kobayashi, and H. Miura, Effects of Aging on Mechanical Properties and Microstructure of Multi-Directionally Forged 7075 Aluminum Alloy, *Mater. Sci. Eng.*, 2017, **700**, p 220–225. https://doi.org/10.1016/J.MSEA.2017.06.017

27. T. Sakai, A. Belyakov, R. Kaibyshev, H. Miura, and J.J. Jonas, Dynamic and Post-Dynamic Recrystallization under Hot, Cold and Severe Plastic Deformation Conditions, *Prog. Mater. Sci.*, 2014, **60**, p 130–207. https://doi.org/10.1016/j.pmatsci.2013.09.002

28. T.R. Praveen, K.R. Gopi, and H.S. Nayaka, Numerical Simulation of Shot Peening Process on Equal Channel Angular Pressed Magnesium Alloy, *Silicon*, 2018, **10**, p 2463–2472. https://doi.org/10.1007/s12633-018-9778-3

29. P.J. Hurley and F.J. Humphreys, The Application of EBSD to the Study of Substructural Development in a Cold Rolled Single-Phase Aluminium Alloy, *Acta Mater.*, 2003, **51**, p 1087–1102. https://doi.org/10.1016/S1359-6454(02)00513-X

30. O. Sitdikov, T. Sakai, A. Goloborodko, H. Miura, and R. Kaibyshev, Grain Refinement in Coarse-Grained 7475 Al Alloy during Severe Hot Forging, *Philos. Mag.*, 2004 https://doi.org/10.1080/14786430412331325049

31. H. Jazaeri and F.J. Humphreys, Quantifying Recrystallization by Electron Backscatter Diffraction, *J. Microsc.*, 2004, **213**(3), p 241–246. https://doi.org/10.1111/j.0022-2720.2004.01296.x

32. M. Suresh, A. Sharma, A.M. More, N. Nayan, and S. Suwas, Effect of Scandium Addition on Evolution of Microstructure, Texture and Mechanical Properties of Thermo-Mechanically Processed Al-Li Alloy AA2195, *J. Alloys Compd.*, 2018, **740**, p 364–374. https://doi.org/10.1016/j.jallcom.2017.12.045

33. R. Kapoor, A. Sarkar, A.N. Behera, and S. Sunil, Materials Science & Engineering A Multi-Axial Forging of Nb-1wt% Zr: Effect of Annealing on Microstructure an Mechanical Properties, *Mater. Sci. Eng. A*, 2020, **772**, p 138805. https://doi.org/10.1016/j.msea.2019.138805

34. M. Suresh, A. Sharma, A.M. More, R. Kalsar, A. Bisht, N. Nayan, and S. Suwas, Effect of Equal Channel Angular Pressing (ECAP) on the Evolution of Texture, Microstructure and Mechanical Properties in the Al-Cu-Li Alloy AA2195, *J. Alloys Compd.*, 2019, **785**, p 972–983. https://doi.org/10.1016/j.jallcom.2019.01.161

35. S.I. Wright, M.M. Nowell, and D.P. Field, A Review of Strain Analysis Using Electron Backscatter Diffraction, *Microsc. Microanal.*, 2011, **17**(3), p 316–329. https://doi.org/10.1017/S1431927611000055

36. K.S. Suresh, N.P. Gurao, S.D. Singh, S. Suwas, K. Chattopadhyay, S.V. Zherebtsov, and G.A. Salishchev, Effect of Equal Channel Angular Pressing on Grain Refinement and Texture Evolution in a Biomedical Alloy Ti13Nb13Zr, *Mater. Charact.*, 2013, **82**, p 73–85. https://doi.org/10.1016/j.matchar.2013.05.003

37. M. Ikeda, K. Kashihara, and T. Aoba, Change in Microstructures and Mechanical Properties during Annealing of AZ31F Magnesium Alloy

Multi-Directionally Forged under Decreasing Temperature Conditions, *J. Jpn. Inst. Light Met.*, 2019, **69**(4), p 228–234. https://doi.org/10.2464/jilm.69.228

38. S. Ramesh, H.S. Nayaka, S. Sahu, K.R. Gopi, M.J. Shivaram, and S. Arya, Influence of Multiaxial Cryoforging on Microstructural, Mechanical, and Corrosion Properties of Copper-Titanium Alloy, *J. Mater. Eng. Perform.*, 2019, **28**(12), p 7629–7641. https://doi.org/10.1007/s11665-019-04454-9

39. S. Vigneshwaran, K. Sivaprasad, R. Narayanasamy, and K. Venkateswarlu, Microstructure and Mechanical Properties of Al – 3Mg – 0.25 Sc Alloy Sheets Produced by Cryorolling, *Mater. Sci. Eng. A*, 2019, **740**, p 49–62. https://doi.org/10.1016/j.msea.2018.10.044

40. H. Dutta and S.K. Pradhan, Microstructure Characterization of High Energy Ball-Milled Nanocrystalline V2O5 by Rietveld Analysis, *Mater. Chem. Phys.*, 2003, **77**(3), p 868–877. https://doi.org/10.1016/S0254-0584(02)00169-4

41. S. Ramesh, G. Anne, G.M. Naik, C. Jagadeesh, and H.S. Nayaka, Microstructural and Mechanical Characterisation of Al-Zn-Mg-Cu Alloy Processed by Multi-Directional Cryo-Forging, *Mater. Today Proc.*, 2021, **46**(12), p 5752–5756. https://doi.org/10.1016/j.matpr.2021.02.70943

42. B. Decreus, A. Deschamps, F. De Geuser, P. Donnadieu, C. Sigli, and M. Weyland, The Influence of Cu/Li Ratio on Precipitation in Al–Cu–Li–x Alloys, *Acta Mater.*, 2013, **61**(6), p 2207–2218. https://doi.org/10.1016/j.actamat.2012.12.041

43. S.G. Mazzini and J.C. Caretti, Effect of Deformation at Elevated Temperature before Age-Hardening on the Mechanical Properties of 2024 Commercial Aluminium Alloy, *Scr. Metall. Mater.*, 1991, **25**(8), p 1987–1990. https://doi.org/10.1016/0956-716X(91)90340-7

44. W. Liang, Q. Pan, Y. He, Y. Li, Y. Zhou, and C. Lu, Effect of Aging on the Mechanical Properties and Corrosion Susceptibility of an Al-Cu-Li-Zr Alloy Containing Sc, *Rare Met.*, 2008, **27**(2), p 146–152. https://doi.org/10.1016/S1001-0521(08)60105-9

45. M. Suresh, R. Kalsar, A.M. More, A. Bisht, N. Nayan, and S. Suwas, Evolution of Microstructure and Texture in the Third Generation Al–Li Alloy AA2195 during Warm Hybrid Processing, *J. Alloys Compd.*, 2021, **855**, p 156750. https://doi.org/10.1016/j.jallcom.2020.156750

46. P.C.S.K. Rajendra and U.G.V. Preetham, Effect of Multi Directional Forging on the Microstructure and Mechanical Properties of Zn-24 Wt % Al-2 Wt % Cu Alloy, *Trans. Indian Inst. Met.*, 2017, **70**(1), p 89–96. https://doi.org/10.1007/s12666-016-0863-2

47. H. Miura and Y. Nakao, Nano-Grained Structure Induced by Mechanical Twinning during Multi-Directional Forging and the Mechanical Properties, *Mater. Sci. Forum.*, 2010, **634**, p 577–593. https://doi.org/10.4028/www.scientific.net/MSF.633-634.577

48. Z. Ye, W. Cai, J. Li, X. Chen, R. Zhang, N. Birbilis, Y. Chen, X. Zhang, P. Ma, and Z. Zheng, Impact of Annealing Prior to Solution Treatment on Aging Precipitates and Intergranular Corrosion Behavior of Al-Cu-Li Alloy 2050, *Metall. Mater. Trans. A.*, 2018, **49**(6), p 2471–2486. https://doi.org/10.1007/s11661-018-4596-1

49. W.J. Kim, C.S. Chung, D.S. Ma, S.I. Hong, and H.K. Kim, Optimization of Strength and Ductility of 2024 Al by Equal Channel Angular Pressing (ECAP) and Post-ECAP Aging, *Scr. Mater.*, 2003, **49**(4), p 333–338. https://doi.org/10.1016/S1359-6462(03)00260-4

50. J. Gubicza, I. Schiller, N.Q. Chinh, J. Illy, Z. Horita, and T.G. Langdon, The Effect of Severe Plastic Deformation on Precipitation in Supersaturated Al–Zn–Mg Alloys, *Mater. Sci. Eng. A*, 2007, **460–461**, p 77–85. https://doi.org/10.1016/j.msea.2007.01.001

51. K. Huang, K. Marthinsen, Q. Zhao, and R.E. Logé, The Double-Edge Effect of Second-Phase Particles on the Recrystallization Behaviour and Associated Mechanical Properties of Metallic Materials, *Prog. Mater. Sci.*, 2018, **92**, p 284–359. https://doi.org/10.1016/j.pmatsci.2017.10.004

52. V. Proton, J. Alexis, E. Andrieu, J.Ô. Delfosse, A. Deschamps, F. De Geuser, M.C. Lafont, and C. Blanc, The Influence of Artificial Ageing on the Corrosion Behaviour of a 2050 Aluminium-Copper-Lithium Alloy, *Corros. Sci.*, 2014, **80**, p 494–502. https://doi.org/10.1016/j.corsci.2016.12.005

53. B. Gable, A. Zhu, A. Csontos, and E. Starke, The Role of Plastic Deformation on the Competitive Microstructural Evolution and Mechanical Properties of a Novel Al–Li–Cu–X Alloy, *J. Light Met.*, 2001, **1**(1), p 1–14. https://doi.org/10.1016/S1471-5317(00)00002-X

54. W.A. Cassada, G.J. Shiflet, and E.A. Starke, The Effect of Plastic Deformation on Al2CuLi (T1) Precipitation, *Metall. Trans. A*, 1991, **22**(2), p 299–306. https://doi.org/10.1007/BF02656799